Numerical Simulation of the CS$_2$-Filled Active Fiber With Flattened All-Normal Dispersion
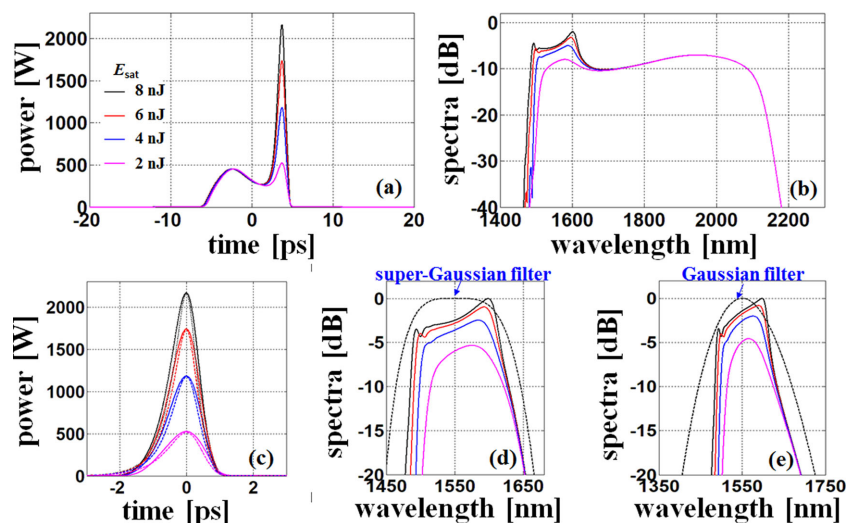
ChunCan Wang
CaiPing Jia
JianFang Yang
MuGuang Wang
JingJing Zheng
Li Pei

Numerical Simulation of the CS$_2$-Filled Active Fiber With Flattened All-Normal Dispersion

ChunCan Wang ⓘ , CaiPing Jia, JianFang Yang, MuGuang Wang ⓘ , JingJing Zheng, and Li Pei ⓘ

Key Laboratory of All Optical Network and Advanced Telecommunication Network, Ministry of Education, Institute of Lightwave Technology, Beijing Jiaotong University, Beijing 100044, China

Abstract: A CS$_2$-filled Er-doped fiber, which can provide high nonlinearity and gain, low and flat all-normal dispersion profile, low loss and single-mode operation in the wavelength range of 1500–2500 nm, is proposed and analyzed by numerical simulation. When the 1900-nm 0.1-ps initial pulse with a peak power of 30 kW is injected into the active fiber, the generated supercontinuum (SC) spectrum has a double-hump structure in the 1550-nm window and covers about 800-nm wavelength range spanning from 1400 to 2200 nm at −20 dB level. Furthermore, the 1550-nm pulse can be obtained synchronously with the 1900-nm initial pulse when the amplified pulse with a temporal double-peak shape is passed through a band-pass filter with its center wavelength at 1550 nm.

Index Terms: Fiber nonlinear optics, supercontinuum generation, fiber lasers.

1. Introduction

Supercontinuum generation (SCG) in the all-normal dispersion fiber can be useful for applications such as optical coherence tomography [1], nonlinear microscopy [2], biophotonic [3], and ultra-short pulse generation [4] due to its perfect coherent properties. Both the passive and active highly nonlinear fibers (HNLFs) with flattened normal dispersion profiles can be employed for the coherent SCG. In the former case, the all-normal dispersion fibers were demonstrated experimentally using the air-silica photonic crystal fibers (PCFs) [4]–[12], or proposed in a numerical study of the heavily germanium-doped silica fiber [13]. The nonlinear parameter of the fiber can be enhanced further for the all-solid soft glass PCF [14]–[16], air-tellurite PCFs [17], tapered tellurite step-index optical fiber [18], As$_2$Se$_3$ chalcogenide glass triangular-core graded-index PCF [19] and hollow-core silica fibers filled with highly nonlinear liquids such as carbon disulfide (CS$_2$) [20]–[25] and chloroform (CHCl$_3$) [26]. In the latter case, the SCG covering from 1064 to beyond 1700 nm with 70-W average output power was demonstrated experimentally using a nonlinear ytterbium-doped fiber amplifier with all-normal dispersion [27]. It was demonstrated by numerical simulation that the SCG with an enhancement of pulse energy and spectral flatness can be obtained through an ytterbium-doped high-nonlinearity normal-dispersion PCF [28]. Recently, the passive HNLF was inserted
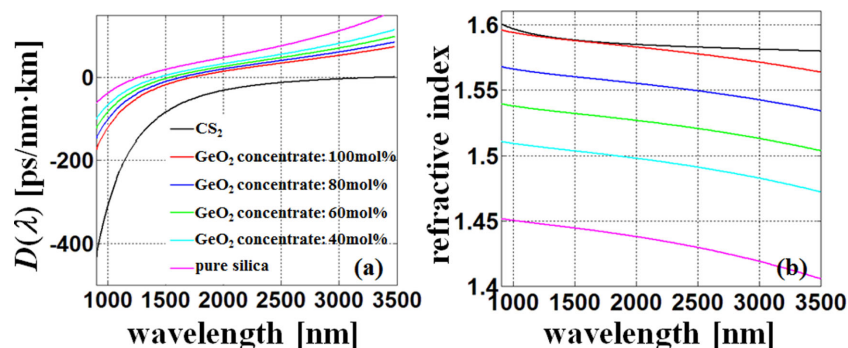
Fig. 1. The curves of material dispersions (a) and refractive indices (b) for CS$_2$, pure silica and GeO$_2$-doped silica with different germanium concentrates.
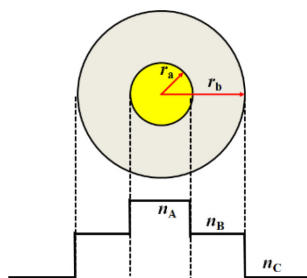

Fig. 2. The cross section of the CS$_2$-filled active fiber. r_a represents the radius of the CS$_2$-filled hollow core, which is surrounded by the inner cladding (gray) with the outer radius of r_b. The inner-cladding region is doped with the rare-earth element and GeO$_2$. n_A, n_B, and n_C are the refractive indices for CS$_2$, GeO$_2$-doped silica and pure silica, respectively.

into the ultrashort pulse mode-locked fiber laser (MLFL) to realize the intracavity SC generation [29]. Furthermore, the real-time transient processes in the MLFLs can be successfully studied by using the time-stretch dispersive Fourier transform (TSDFT) method [30]–[32]. Consequently, it is interesting to investigate the MLFL based on the active HNLF as the gain medium due to its properties of high nonlinearity and gain.

In this paper, an active HNLF with a flattened normal dispersion profile is proposed through designing a CS$_2$-filled Er-doped silica fiber. In Section 2, the properties of the active fiber including the dispersion, nonlinear parameter, loss and gain, are discussed. In Section 3, the evolutions of propagating pulses inside the fiber are studied by numerical simulations, while the influences of the parameters of the fiber and initial pulse are discussed in the spectral and temporal domains.

2. The Properties of the Active CS$_2$-Filled Fiber

As the liquid CS$_2$ exhibits low absorption and high nonlinearity in the visual and near infrared region (NIR), the CS$_2$-filled hollow-core fibers can be used to realize the SCG [21]–[25]. As shown in Fig. 1(a), CS$_2$ shows a broad normal-dispersion wavelength range with a zero dispersion wavelength (ZDW) above 3000 nm, which is desired for designing the all-normal dispersion fibers. Additionally, as shown in Fig. 1(b), the refractive-index difference between CS$_2$ and GeO$_2$-doped silica can be changed by tuning the germanium concentration in the silica, which provides a degree of freedom that make it possible to realize a flat normal dispersion profile through tailoring the waveguide dispersion for the CS$_2$-filled silica fiber. For this reason, as shown in Fig. 2, the hollow core at the center of the fiber is filled with CS$_2$ liquid (yellow region), which is surrounded by the

TABLE 1

The Sellmeier Coefficients for CS$_2$ and GeO$_2$-Doped Silica Glass

C_0	C_1 [10^3nm^2]	C_2 [10^8nm^4]	C_3 [10^{13}nm^6]	C_4 [10^{19}nm^8]	C_5 [10^{-10}nm^{-2}]
1.582445	13.7372	10.0243	-15.6572	1.8294	-3.2117
SA_1	SA_2	SA_3	SI_1	SI_2	SI_3
0.6961663	0.4079426	0.8974794	0.0684043	0.1162414	9.896161
GA_1	GA_2	GA_3	GI_1	GI_2	GI_3
0.80686642	0.71815848	0.85416831	0.068972606	0.15396605	11.841931

GeO$_2$-doped inner cladding (gray ring region) and outer cladding with pure silica. The profiles of the group velocity dispersion (GVD) in the fibers can be tailored by tuning the GeO$_2$ concentrate in the inner cladding, radiuses r_a and r_b. For obtaining optical gain in the 1550-nm wavelength window, the inner cladding of the fiber can be doped with the rare-earth element using dopant ErCl$_3$. As a result, the propagating signal pulses can get energy transferred from pump waves through population inversion and stimulated emission.

2.1 The Dispersion and Nonlinearity in the Fiber

The parameters n_A, n_B and n_C represent the refractive indices of CS$_2$ [33], GeO$_2$-doped silica and pure silica [34], which are given by:

$$n_A^2(\lambda) = C_0 + \frac{C_1}{\lambda^2} + \frac{C_2}{\lambda^4} + \frac{C_3}{\lambda^6} + \frac{C_4}{\lambda^8} + C_5\lambda^2 \tag{1}$$

$$n_{B,\mathrm{orC}}^2(\lambda) - 1 = \sum_{i=1}^{3} \frac{[SA_i + X(GA_i - SA_i)]\lambda^2}{\lambda^2 - [SI_i + X(GI_i - SI_i)]^2} \tag{2}$$

where C_i ($i = 0, 1, \ldots, 5$), and SA_i, SI_i, GA_i and GI_i ($i = 1, 2, 3$), which can be seen in Table 1, are the Sellmeier coefficients for CS$_2$ and GeO$_2$-doped silica glass, respectively. λ is the wavelength in the vacuum, and X is the mole fraction of GeO$_2$ in mol%. When $X = 0$, the refractive index in Eq. (2) is n_C. The GVD is given by

$$D(\lambda) = -\frac{\lambda}{c} \frac{d^2 n_{FM}(\lambda)}{d\lambda^2} \tag{3}$$

where c is the speed of light in vacuum, $n_{FM}(\lambda)$ is the effective index of the fundamental mode (FM) at the operating wavelength λ, which can be obtained by solving the wave equation with the commercial software Comsol. The nonlinearity parameter $\gamma(\lambda)$ is defined as [35]

$$\gamma(\lambda) = \frac{2\pi}{\lambda} \frac{\int \int_{-\infty}^{\infty} n_2(x,y)|\vec{E}_t|^4 dxdy}{(\int \int_{-\infty}^{\infty} |\vec{E}_t|^2 dxdy)^2} \tag{4}$$

where $|\vec{E}_t|$ represents the magnitude of the electric field vector $|\vec{E}_t|$ in the transverse directions. $n_2(x,y)$ is the nonlinear refractive index (NRI). The NRI n_2 of GeO$_2$-doped silica and pure silica are given by ($2.16 + 0.033X$) with the unit of 10^{-20} m^2/W [36]. The NRI n_2 of CS$_2$ is given by [37]

$$n_{2,CS_2} = n_{2,el} + n_{2,nu} = n_{2,el} + \frac{\int I(t) \int h_R(t-t')I(t')dt'dt}{\int I(t)^2 dt} \tag{5}$$

where the nonlinear refractive indices $n_{2,\mathrm{el}}$ and $n_{2,\mathrm{nu}}$ originate from the instantaneous electronic and noninstantaneous nuclear contributions, respectively. $h_R(\mathrm{t})$ is the Raman response function. Since
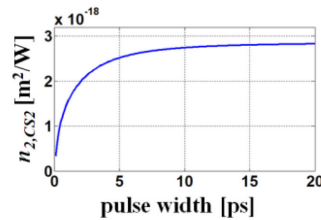
Fig. 3. The values of $n_{2,\mathrm{CS2}}$ when the pulse widths are varied from 0.1 to 20 ps.
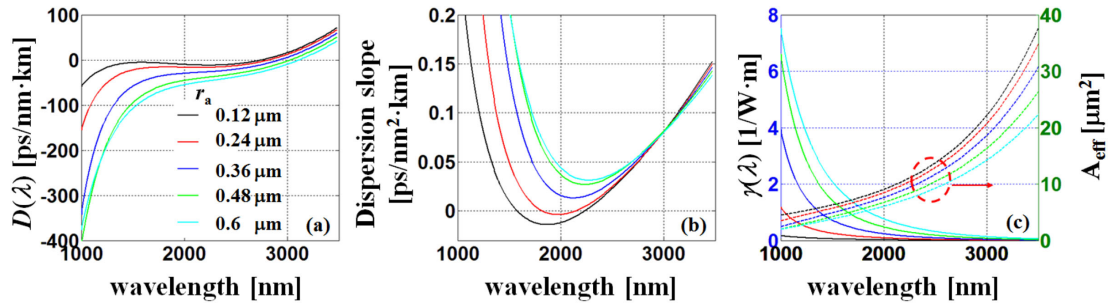

Fig. 4. The curves of GVD $D(\lambda)$ (a), the dispersion slope (b), and the nonlinearity parameter $\gamma(\lambda)$ (left) with effective mode area A_{eff} (right) for different values of r_{a}, where $r_b = 1.4$ μm and $X = 50$ mol%.

I(t) represents temporal intensity of the propagating pulse, $n_{2,\mathrm{CS2}}$ depends on the pulse widths. As shown in Fig. 3, the value of $n_{2,\mathrm{CS2}}$ increases with the input pulse width, and reaches about 2.6×10^{-18} m^2 / W when the pulse width is more than 10 ps. In Section 2, to simplify the analysis, $n_{2,\mathrm{CS2}}$ is taken to be 2.6×10^{-18} m^2 / W because the following discussions focus on the relations between the fiber parameters and the properties of the active CS$_2$-filled fiber. However, the influence of the input pulse duration on the CS$_2$ NRI is taken into account in Section 3.

As shown in Fig. 4(a), when $r_b = 1.4$ μm and $X = 50$ mol%, the CS$_2$-filled fiber shows broadband normal-dispersion regime, where the ZDW shifts from 2750 to 3160 nm with an increase of r_a from 0.12 to 0.6 μm. However, the absolute values of GVD at 1550 nm increase from 6 to 100 ps/nm/km. When $r_a = 0.24$ μm, the GVD profile of the fiber has a wide and flat shape in the wavelength range of 1500–2500 nm, where the dispersion slope is in the range from -0.004 to 0.05 ps/nm^2/km shown in Fig. 4(b). Moreover, as shown in Fig. 4(c), the nonlinear parameters increase with the radius r_a because of a decrease of the mode effective areas A_{eff}. For example, the nonlinear parameters increase from 0.05 to 1.9 W^{-1}•m^{-1} at 1550 nm with increasing r_a from 0.12 to 0.6 μm. Consequently, a trade-off exists between the GVD and nonlinear parameter when choosing the value of the radius r_a. In the following discussion, r_a is set to be 0.24 μm because the fiber has a relatively wide and low GVD profile and high nonlinearity in the normal-dispersion regime.

Furthermore, when r_b is reduced from 1.8 to 0.8 μm, the values of $D(\lambda)$ at 1550 and 2000 nm decrease from 7 and 23 ps/nm/km to -200 and -165 ps/nm/km respectively, as shown in Fig. 5(a). The fiber exhibits a flat and wide normal-dispersion profile in the wavelength range of 1500–2500 nm when 1.0 μm $< r_b <$ 1.4 μm. When r_b increases beyond 1.4 μm, the ZDW has a large blue shift, decreasing from $\sim$2900 nm with $r_b = 1.4$ μm to $\sim$1600 nm with $r_b = 1.6$ μm. As a result, in the latter case the coherent SCG will be limited in the spectral region below 1600 nm. Additionally, as shown in Fig. 5(b), the effective mode area A_{eff} has a large increase with a decrease of r_b in the wavelength region beyond 2000 nm, which results in relatively low nonlinear parameters. This result indicates that the value of r_b should be carefully designed to ensure a large enough ZDW and high nonlinearity for the SCG in the normal dispersion region.

Figure 6 shows the influence of the germanium concentrate X on the GVD and nonlinear parameters when $r_a = 0.24$ μm and $r_b = 1.4$ μm. The fiber with 40 mol% $< X <$ 60 mol% exhibits

Fig. 5. The curves of GVD $D(\lambda)$ (a) and the nonlinearity parameter $\gamma(\lambda)$ (left) with mode effective area A_{eff} (right) (b) for different values of r_b, where $r_a = 0.24$ μm and $X = 50$ mol%.
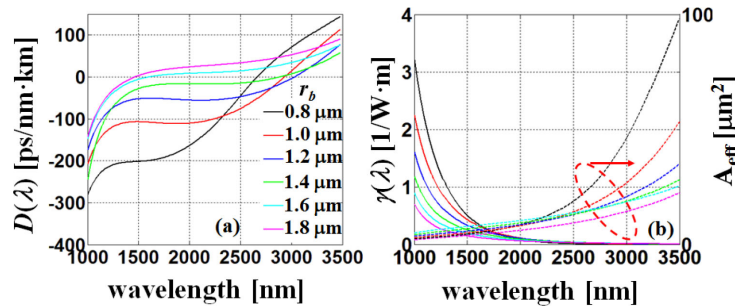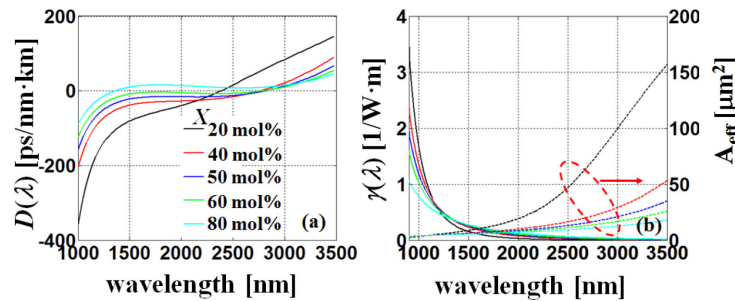

Fig. 6. The curves of GVD $D(\lambda)$ (a) and nonlinear parameter $\gamma(\lambda)$ (left) with mode effective area A_{eff} (right) (b) for the different values of X, where $r_a = 0.24$ μm and $r_b = 1.4$ μm.
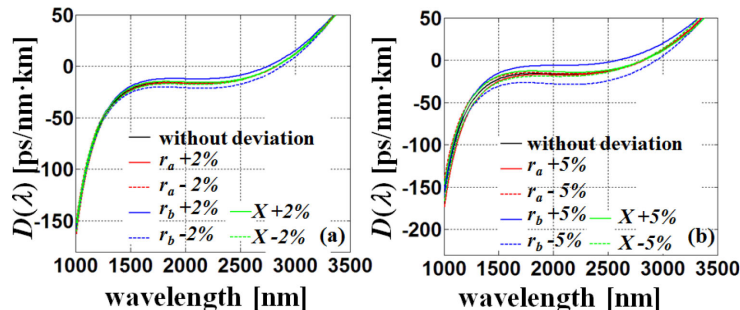

Fig. 7. The GVD curves with and without the deviations of $\pm 2\%$ (a) and $\pm 5\%$ (b) from the parameters r_a, r_b and X. The values of the parameters without deviation are $r_a = 0.24$ μm, $r_b = 1.4$ μm and $X = 50$ mol%.

a flat and low GVD profile ranging from 1500 to 2500 nm with the ZDM of ~2900 nm, while the nonlinear parameter is in the range of 0.2–0.4 W^{-1}•m^{-1} at 1550 nm. However, when X has a further increase or decrease, the ZDM of the fiber has a large blue shift, which is undesired for the SCG in the normal dispersion regime.

Figure 7 shows the influence of the deviation of the parameters on the GVD profiles of the fiber. When the values of r_b are tuned by $\pm 2\%$ or $\pm 5\%$, the variations of the GVD curves in both cases are larger than those when the other parameters are changed. The result indicates that the deviations from the desired geometric parameters need to be carefully controlled within $\pm 2\%$, especially for the radius r_b.

To analyze the role of the CS$_2$-filled core in tailoring the dispersion and nonlinearity, the curves of $D(\lambda)$ and $\gamma(\lambda)$ in the fiber only with a single Ge-doped core are shown in Fig. 8. When the
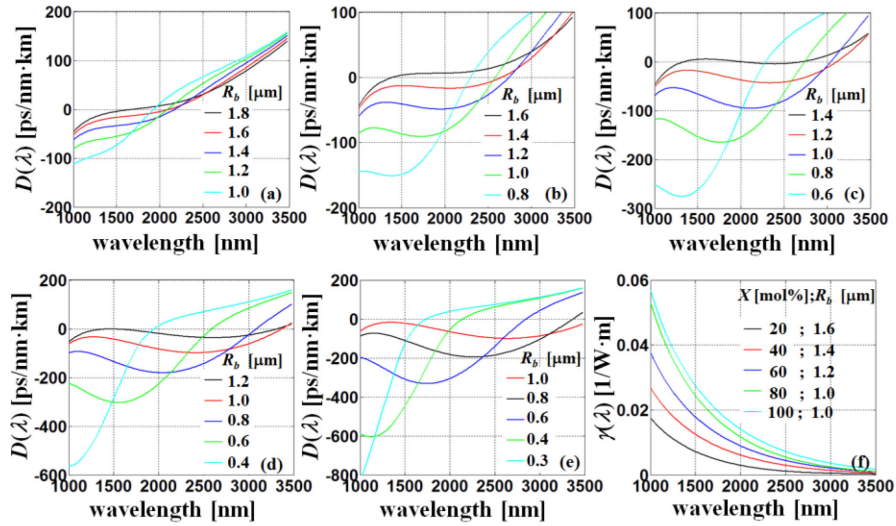
Fig. 8. The GVD profiles with different radius r_b when the values of X are 20 mol% (a), 40 mol% (b), 60 mol% (c), 80 mol% (d) and 100 mol% (e), respectively. (f) The curves of the nonlinearity parameter corresponding to the red curves in Figs. 8(a)–(e), where $r_a = 0$ μm and the normalized frequency V is less than 2.4048 to ensure a single-mode operation in the fiber.

germanium concentration X increases from 20 to 100 mol%, the GVD profiles can be tailored by tuning the radius r_b of the Ge-doped core. It can be seen that the ZDW can shift beyond 3000 nm when $X > 60$ mol%. However, the fiber with a CS$_2$-filled core can provide an additional degree of freedom that can be used to realize a dispersion-flattened fiber in the normal-dispersion regime. Additionally, as shown in Fig. 8(f), the nonlinear parameters of the fibers with relatively flat GVD profiles (red curves in Figs. 8(a)–(e)) are lower by about one order of magnitude than those in the CS$_2$-filled fibers mainly because of the high nonlinearity and refractive index of the CS$_2$ liquid.

2.2 The Loss and Gain in the Fiber

The total loss L_{total} of the optical mode in the fiber includes both confinement loss L_C and the absorption loss L_A. The absorption loss L_A can be written as

$$L_A = \Gamma^{core}(\lambda) \times \alpha_{CS_2} + \Gamma^{ring}(\lambda) \times \alpha_{GeO_2} + \Gamma^{cladding}(\lambda) \times \alpha_{SiO_2} \tag{6}$$

where the parameters $\Gamma^{core}(\lambda)$ and $\Gamma^{cladding}(\lambda)$ are the fractions of optical power in the CS$_2$-filled core and silica cladding, respectively. Moreover, α_{cs2}, α_{GeO2} and α_{SiO2} represent the absorption losses in CS$_2$, GeO$_2$ and pure-silica [38]–[40], respectively. The confinement loss L_C is given by

$$L_c = \frac{20}{\ln(10)} \frac{2\pi}{\lambda} Im(n_{eff}) \quad dB/m \tag{7}$$

where $Im(n_{eff})$ represents the imaginary part of the effective index of the mode.

For the fibers by doping the active area with rare-earth elements, the gain characteristic is closely related to the absorption spectrum $\alpha_A(\lambda)$ and gain spectrum $g(\lambda)$, which are given by [41]

$$\alpha_A(\lambda) = \Gamma^{ring}(\lambda)\sigma_a(\lambda)N_t \tag{8}$$

$$g(\lambda) = \Gamma^{ring}(\lambda)\sigma_e(\lambda)N_t \tag{9}$$

where N_t is the doping concentrate of rare-earth element, $\Gamma^{ring}(\lambda)$ is the overlap factor representing the fraction of optical power within the ring-shape active area, i.e., the inner cladding of the fiber. $\sigma_a(\lambda)$ and $\sigma_e(\lambda)$ are the absorption and emission cross sections at wavelength λ, respectively.
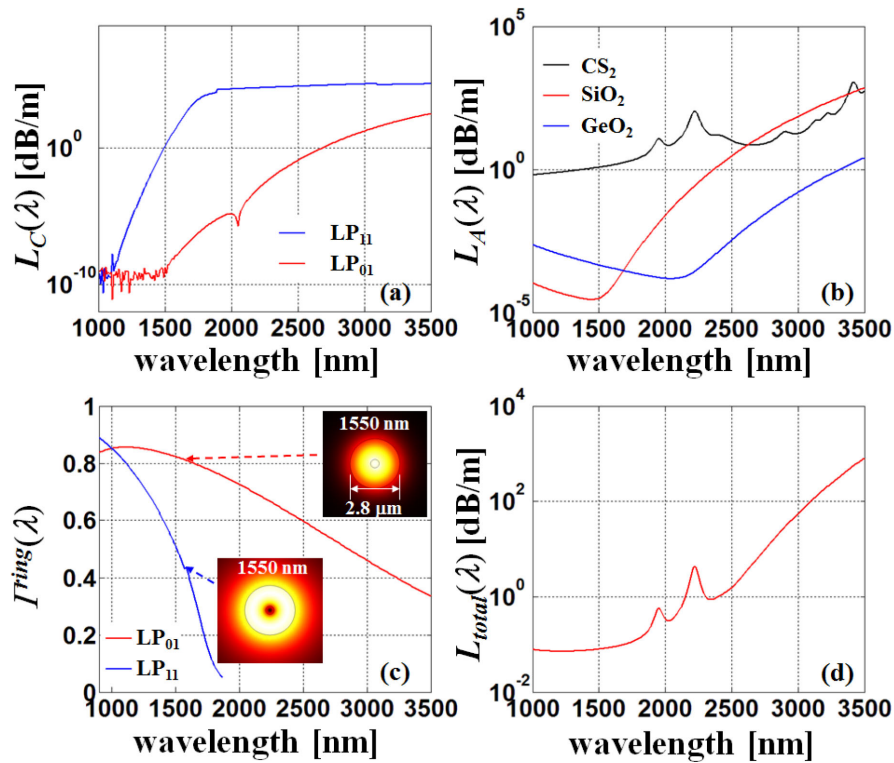
Fig. 9. The curves of confinement losses L_C for the FM LP$_{01}$ and first-order high mode LP$_{11}$ (a), absorption losses L_A (b), the overlap integral $\Gamma^{ring}(\lambda)$ in the inner cladding (c), and total loss L_{total} for the FM LP$_{01}$ (d), where $r_a = 0.24$ μm, $r_b = 1.4$ μm and $X = 50$ mol%. The insets in (c) show the mode intensity profiles of the modes LP$_{01}$ and LP$_{11}$ at 1550 nm.
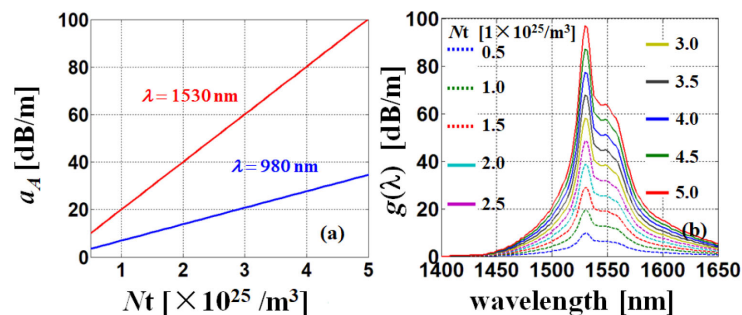

Fig. 10. The absorptions α_A at the wavelengths of 980 (blue) and 1530 nm (red) as functions of the density of erbium ions N_t with $\sigma_a = 1.879 \times 10^{-25}$ m^2 (980 nm) and 5.5×10^{-25} m^2 (1530 nm) [42] (a), and gain spectra $g(\lambda)$ for the FM LP$_{01}$ in the CS$_2$-filled active fiber with different values of N_t (b), when $r_a = 0.24$ μm, $r_b = 1.4$ μm and $X = 50$ mol%.

As show in Fig. 9(d), the total loss of the FM LP$_{01}$ in the fiber is much less than 1 dB/m at most wavelengths ranging from 970 nm to 2500 nm except for a absorption peak near 2250 nm in CS$_2$ seen in Fig. 9(b). Furthermore, as shown in Fig. 9(a), the confinement loss for the first-order high mode LP$_{11}$ is much larger than that for the FM LP$_{01}$ when $\lambda > 1500$ nm, indicating that the fiber can support a single-mode operation in this wavelength range. For the Er-doped fiber, the 980-nm and 1480-nm single-mode laser diodes can be used as the pumping sources. When $\lambda = 980$ nm, the CS$_2$-filled active fiber supports both the modes LP$_{01}$ and LP$_{11}$. However, as shown in Fig. 9(c), the values of Γ^{ring} are above 0.8 in both cases. As a result, as show in Fig. 10(a), the absorption
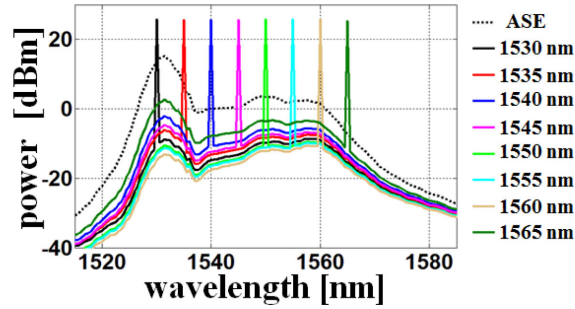
Fig. 11. The output powers for the signal lights with different wavelengths (solid) and ASE (dotted) without input signals, where the forward- and backward-pumping powers are 300 mW, fiber length is 1 m and initial signal power is −10 dBm.

α_A in Eq. 8 at the wavelengths of 980 and 1530 nm can reach 30 and 90 dB/m when N_t is 5 × 10^{25}/m^3. As the wavelength is increased, the optical mode field is confined less and less as it extends farther into the outer cladding. Consequently, Γ^{ring} decreases with the wavelengths shown in Fig. 9(c). However, the values of Γ^{ring} for the FM are more than 0.48 over a broad wavelength range from 970 to 2800 nm, which is helpful to obtain high gain and absorption spectra for the Er-doped fibers. For example, the gain $g(\lambda)$ at 1550 nm shown in Fig. 10(b) can be more than 60 dB/m, which indicates that the CS$_2$-filled fiber with an Er-doped ring region can provide high enough gain in the 1550-nm window.

Furthermore, for the Er-doped fiber amplifier pumped at 980 nm in the steady state condition, the population density in the upper level along the fiber can be expressed as [43]

$$N_2(z) = \cfrac{\cfrac{\Gamma_p^{ring}\lambda_p\sigma_a(\lambda_p)N_T[P_p^+(z)+P_p^-(z)]}{hcA_{ring}} + \cfrac{\sum_{k=1}^{K}\Gamma_s^{ring}\lambda_{sk}\sigma_a(\lambda_{sk})N_T P_{sk}(z)}{hcA_{ring}}}{\cfrac{\Gamma_p^{ring}\lambda_p[\sigma_a(\lambda_p)+\sigma_e(\lambda_p)][P_p^+(z)+P_p^-(z)]}{hcA_{ring}} + \cfrac{\sum_{k=1}^{K}\Gamma_s^{ring}\lambda_{sk}[\sigma_a(\lambda_{sk})+\sigma_e(\lambda_{sk})]P_{sk}(z)}{hcA_{ring}} + \cfrac{1}{\tau}} \tag{10}$$

where the upper-level population density $N_2(z)$ depends on the powers of signal $P_{sk}(z)$, forward and backward propagating pump lights $P_p^+(z)$ and $P_p^-(z)$, respectively. λ_p and λ_{sk} are the wavelengths of pump and signal lights. τ is the upper level lifetime, h is Planck's constant, c is the speed of light in vacuum. Γ_p^{ring} and Γ_s^{ring} are the power filling factors for the pump and signal wavelengths in the Er-doped region, whose area is A_{ring}. z is the position along the fiber. The power distributions along the fiber for the signal and pump lights can be obtained by the rate equations as follows

$$\frac{dP_p^{\pm}(z)}{dz} = \pm\{\Gamma_p^{ring}[(\sigma_e(\lambda_p)+\sigma_a(\lambda_p))N_2(z)-\sigma_a(\lambda_p)N_T]P_p^{\pm}(z)\} \tag{11}$$

$$\frac{dP_{sk}(z)}{dz} = \Gamma_s^{ring}[(\sigma_e(\lambda_{sk})+\sigma_a(\lambda_{sk}))N_2(z)-\sigma_a(\lambda_{sk})N_T]P_{sk}(z)-\alpha P_{sk}(z)+2h\nu_k\Delta\nu_k\sigma_e(\lambda_{sk})N_2(z) \tag{12}$$

where the last term of the right side in Eq. (12) represents the amplified simultaneous emission (ASE) power, $\Delta\nu_k$ is the ASE bandwidth. α is the linear loss with a unit of m^{-1}, which is identical to the loss L_{total} in dB/m unit shown in Fig. 9(d). The term $2h\nu_k\Delta\nu_k$ denotes the spontaneous emission contribution from the local population N_2. In solving the rate equations, the parameters are set by λ_p = 980 nm, τ = 10 ms, A_{ring} = 5.98 μm^2, Γ_p = 0.85, Γ_s = 0.80 and N_T = 5 × 10^{25} m^{-3}. The rate equations of Eqs. 10–12 can be solved numerically by using the fourth-order Runge-Kutta method.

As shown in Fig. 11, the −10-dBm initial signals with wavelengths ranging from 1530 to 1565 nm can be amplified to about 26 dBm in the gain fiber, corresponding to at least 35 dB/m of signal gain.

3. Numerical Simulation of the Supercontinuum Generation

The evolutions of the propagating pulses can be described by the generalized nonlinear Schrödinger equation (GNLSE), which takes into accounts the effects of dispersion, nonlinearity, loss and gain in the fiber [35]:

$$\frac{\partial A}{\partial z} + \frac{\alpha}{2} - \frac{g}{2}A - \sum_{n\geq2}\frac{i^{n+1}}{n!}\beta_n\frac{\partial^n A}{\partial T^n} = i\gamma\left(1+i\tau_{shock}\frac{\partial}{\partial T}\right)$$

$$\times\ [A(z,T))\int_0^\infty R(t')|A(z,T-t')|^2 dt'] \tag{13}$$

where $A(z, T)$ represents the slowly varying pulse envelope in time domain. The initial pulse can be assumed to be a Gaussian pulse, i.e., $A(0, T) = \sqrt{P0}exp(-T^2/2T_0^2)$, where $T_0 = T_{FWHM}$ $\sqrt{2ln2}$; T_{FWHM} is the full width at half-maximum (FWHM) pulse duration; and peak power P_0 can be obtained by $P_0 = 0.94\ E_0\ /\ T_{FWHM}$, where E_0 is the pulse energy. β_n are the dispersion coefficients associated with the Taylor series expansion of the propagation constant $\beta(\omega)$ at the center frequency ω_0. In the process of solving GNLSE, the dispersion operator in the frequency domain is applied through multiplication of the complex spectral envelope $\tilde{A}(z, \omega)$ by the operator $\beta(\omega)–(\omega\ -\omega0)\beta_1–\beta_0$. z is the propagation distance. T is the retarded time for a comoving frame at the group velocity $1/\beta_1$. γ is the nonlinear parameter. The time derivative term on the right-hand side models the dispersion of the nonlinearity, which is associated with the effects of self-steepening and optical shock formation, characterized by a time scale $\tau_{\rm shock} = 1/\omega_0$. The nonlinear response function $R(T) = (1-f_R)\delta(t)+ f_R h_R(t)$, including both instantaneous and delayed Raman contributions. The fractional contribution of the delayed Raman response to nonlinear polarization $f_{\rm R}$ is given by [38]

$$f_R = \frac{n_{2,nu}}{n_{2,el}+n_{2,nu}} \tag{14}$$

The gain coefficient g is given by [44]:

$$g = \frac{g_0}{1+E_{pulse}/E_{sat}+(\omega-\omega_0)^2/\Delta\omega_g^2}. \tag{15}$$

where the parameter g_0 related to the doping concentration is small-signal gain at the center wavelength of 1550 nm, E_{pulse} is the pulse energy, E_{sat} is the gain saturation energy which is pump-power dependent. $\Delta\omega_g$ is the gain bandwidth, which corresponds to the wavelength bandwidth of 40 nm for the Er-doped fiber. In the following discussions, the values of g_0 are in the range of 0–8 m^{-1}, which is feasible according to the results shown in Figs. 10 and 11. Although the normal dispersion fiber does not support solitons, the solitons number given by Eq. 16 is useful for interpreting the results:

$$N = \sqrt{\frac{L_D}{L_N}} = \sqrt{\frac{T_{FWHM}^2\gamma P_0}{|\beta_2|}} \tag{16}$$

where the dispersion length L_D and the nonlinear length L_N are $L_D = T_{FWHM}^2\ /\ |\beta_2|$ and $L_N = 1/\gamma/P_0$, respectively.

3.1 The Case of the 1550-nm Initial Pulse

When the CS2-filled fiber is pumped by 1550-nm pulses, $P_0 < 3$ kW is required for avoiding the bubble formation likely due to the effect of multi-photon absorption (MPA) [21]. However, the MPA issue can be overcome by pumping at longer wavelengths. For example, no damage behavior was observed when 1900-nm pulses with peak powers of up to 30 kW was coupled into the CS2-filled fiber [38]. Recently, Schaarschmidt et al. reported that the 110-fs 1900-nm pulses with high average power of up to 1 W can transmit through the CS$_2$-filled silica fiber without any degradation and
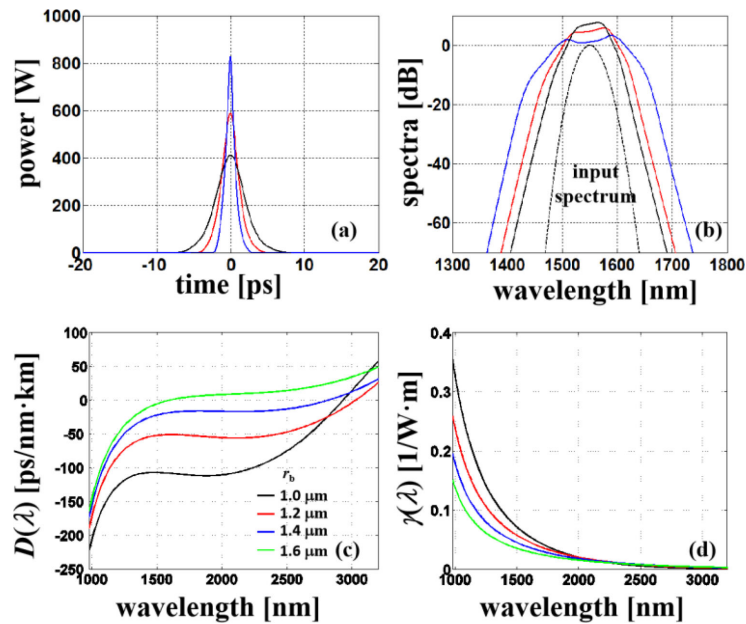
Fig. 12. The output pulses in the temporal (a) and spectral (b) domains from the 0.6-m fiber with the curves of the dispersion $D(\lambda)$ (c) and nonlinear parameter γ (λ) (d) for the different r_b, where $\lambda_0 = 1550$ nm, $T_{FWHM} = 0.1$ ps, $P_0 = 2$ kW, $E_{sat} = 1$ nJ, $g_0 = 6$ m^{-1}, $r_a = 0.24$ μm and $X = 50$ mol%.
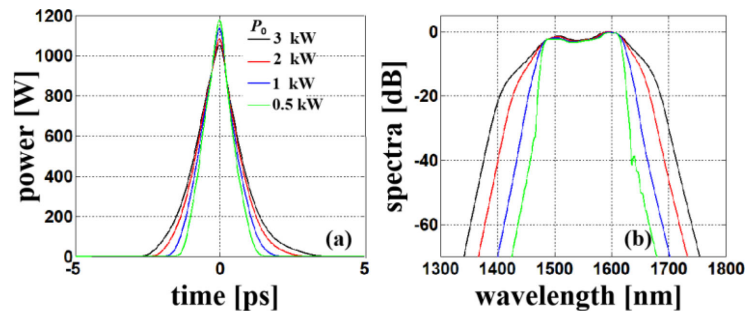

Fig. 13. The output pulses in the temporal (a) and spectral (b) domains from the 1-m fiber for the initial pulses with different P_0, where $\lambda_0 = 1550$ nm, $T_{FWHM} = 0.1$ ps, $E_{sat} = 1$ nJ, $g_0 = 8$ m^{-1}, $r_a = 0.24$ μm, $r_b = 1.4$ μm and $X = 50$ mol%.

obtained the supercontinuum generation spanning from 1300 to 2500 nm [45]. Consequently, in the following discussions, the peak powers of initial pulses are lower than 3 and 30 kW for the 1550- and 1900-nm pulses due to the bubble formation issue.

As shown in Figs. 12(c) and (d), increasing the radius r_b can lower the absolute values of GVD in the normal dispersion regime, and result in a decrease of nonlinear parameter. The pulse propagating along the fiber with $r_b = 1.4$ μm exhibits a higher peak power and broader spectrum due to the stronger nonlinearity-induced spectral broadening combined with the weaker GVD effect, compared with the cases of $r_b = 1.2$ and 1.0 μm, as shown in Figs. 12(a) and (b). For this reason, r_b is chosen to be 1.4 μm in the following discussion.

When the peak power of the 0.1-ps input pulse increases from 0.5 to 3 kW, the 20-dB spectral width of the output pulse is broadened from 160 (1470–1630 nm) to 290 nm (1400–1690 nm), as shown in Fig. 13(b). At the same time, T_{FWHM} of the output pulse increases from 1 to 1.4 ps due to the GVD-induced pulse broadening. However, the peak powers of the output pulses in all cases remain near 1.1 kW due to the fixed E_{sat} and g_0 of the active fiber.
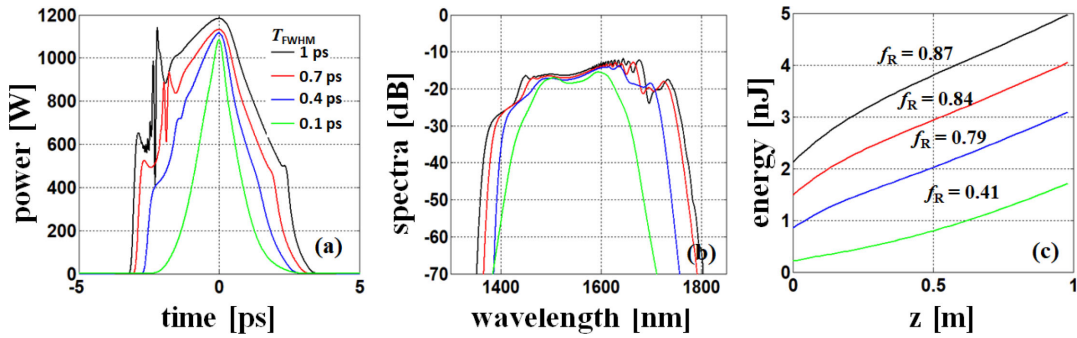
Fig. 14. The output pulses in the temporal (a) and spectral (b) domains from the 1-m fiber, and the pulse energies as a function of the propagating distance z (c) for the input pulses with different T_{FWHM}, where $\lambda_0 = 1550$ nm, $P_0 = 2$ kW, $E_{sat} = 1$ nJ, $g_0 = 8$ m^{-1}, $r_a = 0.24$ μm, $r_b = 1.4$ μm and $X = 50$ mol%.
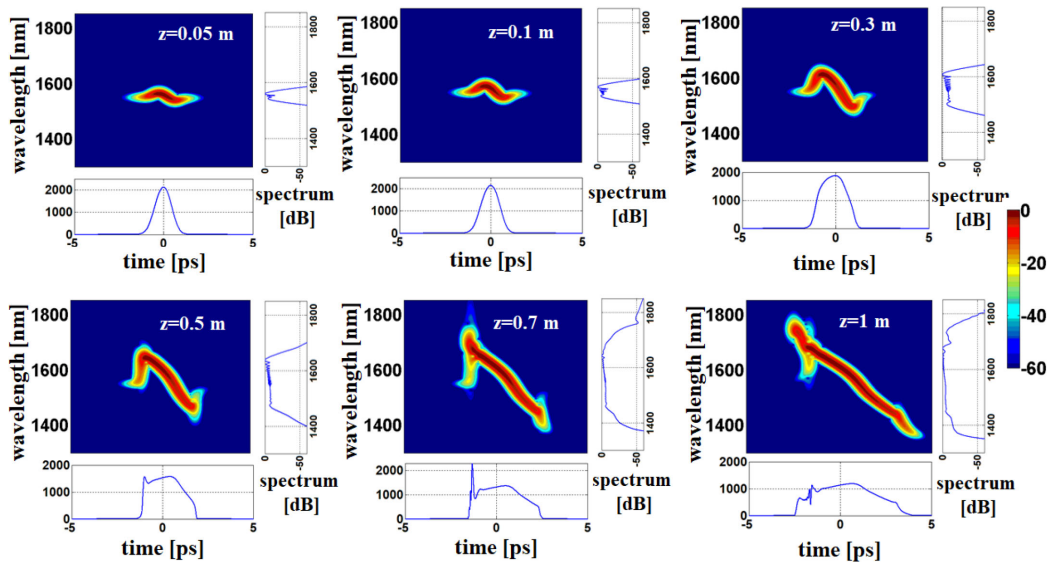

Fig. 15. The spectrograms of the propagating pulses at z = 0.05, 0.1, 0.3, 0.5, 0.7 and 1 m, respectively. $\lambda_0 = 1550$ nm, $T_{FWHM} = 1$ ps, $P_0 = 2$ kW, $g_0 = 8$ m^{-1}, $E_{sat} = 1$ nJ, $r_a = 0.24$ μm, $r_b = 1.4$ μm and $X = 50$ mol%. The length of optical WB $L_{WB} = 0.4$ m.

When the duration T_{FWHM} of the 2-kW initial pulse is increased from 0.1 ($N = 6$) to 1 ps ($N = 103$), the 20-dB spectral width of the output pulse increases from 250 (1420–1670 nm) to 400 nm (1370–1770 nm) because that, the spectral broadening can be enhanced by increasing the dispersion length L_d (from 0.39 to 39.2 m at 1550 nm) and γ (from 0.05 to 0.19 W^{-1}/m at 1550 nm). However, as shown in Figs. 14(a) and (b), the pulse profiles both in the temporal and spectral domains exhibit the rapid oscillations on the leading and trailing edges when T_{FWHM} is > 0.7 ps. In addition, as shown in Fig. 14(c), the pulses have an increase of the pulse energy with the propagation distance although the SRS can lead to the energy loss.

Figures 15 and 16 show the evolutions of the propagating pulses along the fiber for the 1- and 0.1-ps initial pulses, respectively. In the former case, the pulse during early stage of propagation exhibits a spectral broadening mainly because of the effect of self-phase modulation (SPM). In the normal GVD regime, the SPM-induced red- and blue-shifted frequency components interfere the unshifted lights on the leading and trailing regions of the pulse respectively, resulting in the
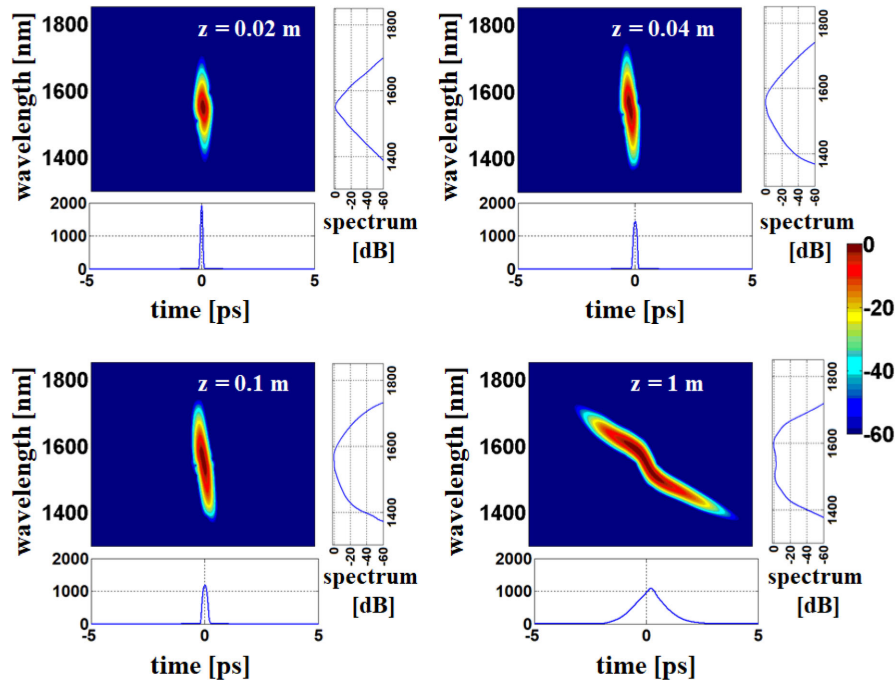
Fig. 16. The spectrograms of the propagating pulses at z = 0.02, 0.04, 0.1 and 1 m, respectively. $\lambda_0 =$ 1550 nm, $T_{FWHM} = 0.1$ ps, $P_0 = 2$ kW, $g_0 = 8$ m^{-1}, $E_{sat} = 1$ nJ, $r_a = 0.24$ μm, $r_b = 1.4$ μm and $X = 50$ mol%. The length of optical WB $L_{WB} = 0.08$ m.

phenomenon of the optical wave breaking (WB). Since the length of the optical WB is given by $L_{WB} = 1.1L_D/N$ [46], when the propagation distance increases beyond 0.4 m of L_{WB}, the pulse spectrum has a further broadening through the four-wave mixing (FWM) due to the onset of the optical WB, and remains nearly unchanged on the blue side when the propagation distance z is > 0.7 m. However, the new spectral components on the red side are created continuously due to the strong effect of SRS on the leading edge of the pulse, where deep oscillation structures developed by the interference between different frequency components distort the pulse shape. Furthermore, since 39.2 m of L_D is much longer than the fiber length, the GVD effect is too weak to make the frequency components located at a unique temporal position in time, which can also explain the presence of oscillation structures across the pulse.

In the latter case with $N = 6$, $L_{WB} = 0.08$ m and $L_D = 0.39$ m, the pulse spectrum is broadened through the effects of SPM and subsequent FWM, and reaches its maximum 20-dB bandwidth ranging from 1420 to 1660 nm after about 0.1 m. When z is > 0.1 m, the pulse exhibits nearly unchanged spectral bandwidth and GVD-induced pulse broadening. Furthermore, the spectrogram shows that each wavelength components is located at a unique temporal position across the pulse, which explains why the pulse is free of interference fine structures.

Furthermore, as shown in Figs.17 and 18, the output pulses show an increase of peak powers and a temporal narrowing by increasing the values of g_0 and E_{sat}, while the pulse spectra exhibit an intensity growth in the 1550-nm wavelength window. An interesting feature of the output spectra is that the spectral profiles exhibit a double-hump structure in the 1550-nm window. Since the amplified pulse has a relatively higher peak power compared with that in the case of passive fiber ($g_0 = 0$ m^{-1}), the energy transferring from the center wavelength of 1550 nm to the blue and red sides induced by the effect of FWM can be enhanced. As a result, two spectral sidelobs with center wavelength of 1550 nm is formed, while the effect of SRS leads to the higher peak intensity on the red side. Additionally, as shown in Fig. 17(b) and Fig. 18(b), for an initial pulse with the given peak
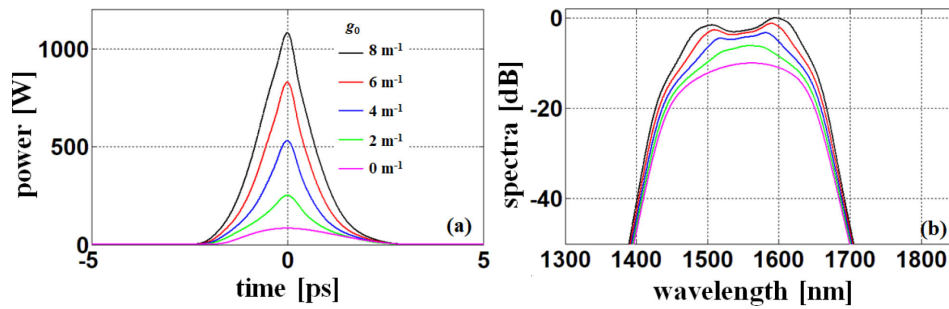
Fig. 17. The output pulses in the temporal (a) and spectral (b) domains from the 1-m fiber for the different values of g_0, where $\lambda_0 = 1550$ nm, $T_{FWHM} = 0.1$ ps, $P_0 = 2$ kW, $E_{sat} = 1$ nJ, $r_a = 0.24$ μm, $r_b = 1.4$ μm and $X = 50$ mol%.
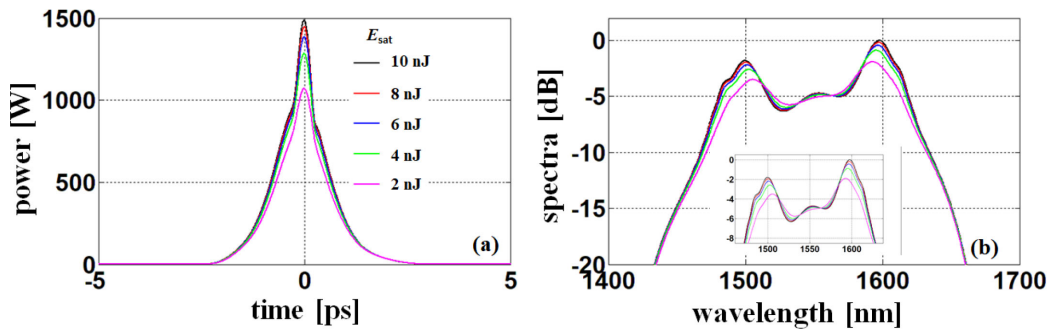

Fig. 18. The output pulses in the temporal (a) and spectral (b) domains from the 1-m fiber for the different values of E_{sat}, where $\lambda_0 = 1550$ nm, $T_{FWHM} = 0.1$ ps, $P_0 = 2$ kW, $g_0 = 6$ m^{-1}, $r_a = 0.24$ μm, $r_b = 1.4$ μm and $X = 50$ mol%.

power and duration, the 10-dB spectral widths of the output pulses remain nearly unchanged in both cases. The results indicate that for the pulses propagating inside the CS$_2$-filled Er-doped fiber, an increase in the concentration of the rare-earth ions or pump powers can raise the pulse energy and peak power, but has a negligible influence on the spectral bandwidth, which is mainly dependent on the peak power and duration of the initial pulse, and nonlinear parameter and dispersion of the fiber.

3.2 The Case of the 1900-nm Initial Pulse

So far the case of the initial pulse with $\lambda_0 = 1550$ nm is discussed. Since the ultrashort pulse lasers based on the Tm-doped fibers can provide high energy pulses in the 1900-nm wavelength window, Figure 19 shows the output pulses from the CS$_2$-filled Er-doped fiber by using the 1900-nm pulses with $T_{FWHM} = 0.1$ ps as a seeding source. When $P_0 = 30$ kW, the output pulse has a 20-dB spectral width of ~ 800 nm ranging from 1400 to 2200 nm. Additionally, the temporal shapes of the output pulses exhibit a double-peak structure due to the gain characteristic of the Er-doped fiber, where the peaks on the trailing edge result from the amplified frequency components within the gain spectrum.

Furthermore, as shown in Figs. 20(a) and (b), the peak powers on the trailing edge and corresponding spectral parts near 1550 nm of the output pulses can be effectively amplified by increasing E_{sat}. Consequently, the pulse with center wavelength of 1550 nm can be obtained when the amplified pulse at the output of the Er-doped fiber is spectrally filtered by the filters with the 1550-nm center wavelength, as shown in Figs. 20(c), (d) and (e). The shapes of the spectral filter are taken to be a super-Gaussian $H_1(\omega) = \exp[-\omega^4/(\Delta\omega_f^4)]$ and Gaussian $H_2(\omega) = \exp[-\omega^2/(\Delta\omega_f^2)]$,
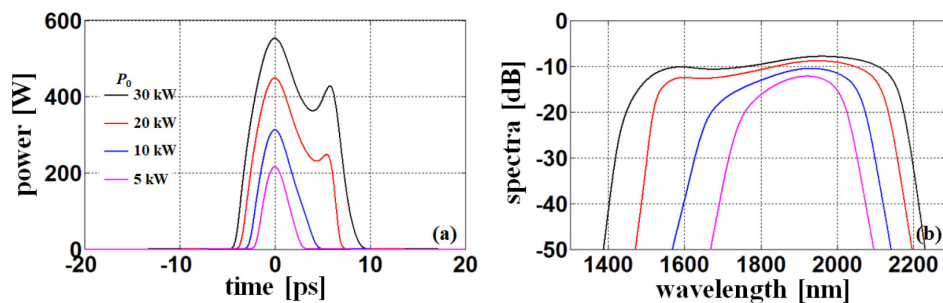
Fig. 19. The output pulses in the temporal (a) and spectral (b) domains from the 1-m fiber for the input pulses with different P_0, where $\lambda_0 = 1900$ nm, $T_{FWHM} = 0.1$ ps, $E_{sat} = 1$ nJ, $g_0 = 8$ m^{-1}, $r_a = 0.24$ μm, $r_b = 1.4$ μm and $X = 50$ mol%.
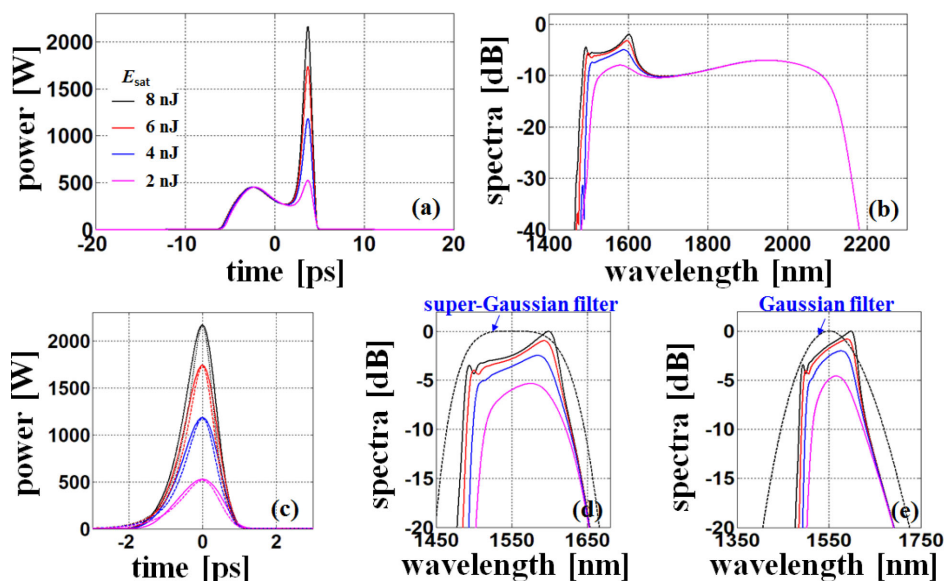

Fig. 20. The output pulses from the 1-m fiber with the different E_{sat} in the temporal (a) and spectral (b) domains. The temporal intensities of pulses from the spectral filters with super-Gaussian (solid) and Gaussian spectral (dotted) shapes (c) and corresponding output pulse spectra (d)(e), where $\lambda_0 = 1900$ nm, $P_0 = 20$ kW, $T_{FWHM} = 0.1$ ps, $g_0 = 8$ m^{-1}, $r_a = 0.24$ μm, $r_b = 1.4$ μm and $X = 50$ mol%.

where $\Delta\omega_f$ represents the frequency bandwidth. When $\Delta\omega_f = 57.69$ THz (corresponding to a wavelength bandwidth of 60 nm), the output pulses from the Gaussian filter have relatively longer leading edges in the temporal domains due to theirs broader trailing edges in the spectral domains than those from the super-Gaussian filter. The result indicates that the CS$_2$-filled Er-doped fiber can provide an interesting approach for generating a 1550-nm pulse synchronously by using the 1900-nm ultrashort pulse as an initial light source.

4. Conclusion

The CS$_2$-filled Er-doped fiber with an appropriate geometric size and refractive-index distribution can provide high nonlinearity, flattened all-normal dispersion and gain in the 1550-nm window. The numerical results show that, when $r_a = 0.24$ μm, $r_b = 1.4$ μm and $X = 50$ mol%, the fiber with $D(\lambda) = -20$ ps/nm/km at 1550 nm has a wide and flat GVD profile in the wavelength range of

1500–2500 nm, where the dispersion slope is in the range from -0.004 to 0.05 ps/nm^2/km. The value of nonlinear parameter $\gamma(\lambda)$ at 1550 nm increases from 0.05 to 0.19 W^{-1}/m when the duration T_{FWHM} of initial pulse increases from 0.1 to 1 ps. Additionally, the gain $g(\lambda)$ at 1550 nm can reach 60 dB/m for the CS$_2$-filled fiber with an Er-doped inner cladding, while the fiber can support a single-mode operation with $\lambda > 1500$ nm because the confinement loss of the mode LP$_{11}$ is much larger than that of the FM LP$_{01}$.

Furthermore, the SCG based on the CS$_2$-filled Er-doped fiber is simulated numerically with the 1550-nm and 1900-nm pulses as the initial pulse sources. In the former case, the output pulse spectrum with 20-dB spectral range of 1400–1690 nm can be obtained when $P_0 = 3$ kW and $T_{FWHM} = 0.1$ ps for the initial pulse. When T_{FWHM} of the initial pulse is > 0.7 ps, the presence of oscillation structures in both temporal and spectral domains severely distorts the pulse shape because of the strong effect of SRS. In addition, an increase of g_0 and E_{sat} can increase the peak power and energy of the output pulse with a decrease of pulse duration in the temporal domain. At the same time, the pulse spectrum exhibits a double-hump structure in the 1550-nm window due to the combined effect of gain and FWM, which can lead to a double-peak temporal shape of the output pulse in the latter case. Additionally, it had been demonstrated experimentally that the hollow-core fibers with the core diameters of 1.8 and 5 μm can be filled with CS2 liquid by capillary action without other special equipment [21], [22]. Although a decrease of the hollow-core diameter will slow down the filling process, the nano-scale hollow channel can be filled by using the pressure-assisted filling technique [47]. Consequently, it is feasible to fabricate the CS$_2$-filled gain fiber, which can be used to generate the 1550-nm pulses synchronously with the 1900-nm initial pulse by spectrally filtering the amplified supercontinuum spectrum.

Acknowledgment

References

[1] B. Povazay *et al.*, "Submicrometer axial resolution optical coherence tomography," *Opt. Lett.*, vol. 27, no. 20, pp. 1800–1802, 2002.

[2] H. N. Paulsen, K. M. Hilligse, J. Thøgersen, S. R. Keiding, and J. J. Larsen, "Coherent anti-stokes Raman scattering microscopy with a photonic crystal fiber based light source," *Opt. Lett.*, vol. 28, no. 13, pp. 1123–1125, 2003.

[3] H. Tu and S. A. Boppart, "Coherent fiber supercontinuum for biophotonics," *Laser Photon. Rev.*, vol. 7, no. 5, pp. 628–645, 2013.

[4] A. M. Heidt *et al.*, "High quality sub-two cycle pulses from compression of supercontinuum generated in all-normal dispersion photonic crystal fiber," *Opt. Exp.*, vol. 19, no. 15, pp. 13873–13879, 2011.

[5] L. E. Hooper, P. J. Mosley, A. C. Muir, W. J. Wadsworth, and J. C. Knight, "Coherent supercontinuum generation in photonic crystal fiber with all-normal group velocity dispersion," *Opt. Exp.*, vol. 19, no. 6, pp. 4902–4907, 2011.

[6] A. Hartung, A. M. Heidt, and H. Bartelt, "Pulse-preserving broadband visible supercontinuum generation in all-normal dispersion tapered suspended-core optical fibers," *Opt. Exp.*, vol. 19, no. 13, pp. 12275–12283, 2011.

[7] A. M. Heidt *et al.*, "Coherent octave spanning near-infrared and visible supercontinuum generation in all-normal dispersion photonic crystal fibers," *Opt. Exp.*, vol. 19, no. 4, pp. 3775–3787, 2011.

[8] I. A. Sukhoivanov, S. O. Iakushev, O. V. Shulika, J. A. Andrade-Lucio, A. Díez, and M. Andrés, "Supercontinuum generation at 800 nm in all-normal dispersion photonic crystal fiber," *Opt. Exp.*, vol. 22, no. 24, pp. 30234–30250, 2014.

[9] H. H. Tu *et al.*, "Scalar generalized nonlinear schrödinger equation-quantified continuum generation in an all-normal dispersion photonic crystal fiber for broadband coherent optical sources," *Opt. Exp.*, vol. 18, no. 26, pp. 27872–27884, 2010.

[10] I. A. Sukhoivanov, S. O. Iakushev, O. V. Shulika, E. Silvestre, and V. A. Miguel, "Design of all-normal dispersion microstructured optical fiber on silica platform for generation of pulse-preserving supercontinuum under excitation at 1550 nm," *J. Lightw. Technol.*, vol. 35, no. 17, pp. 3772–3779, 2017.

[11] A. M Heidt, "Pulse preserving flat-top supercontinuum generation in all-normal dispersion photonic crystal fibers," *J. Opt. Soc. Amer. B Opt. Phys.*, vol. 27, no. 3, pp. 550–559, 2010.

[12] A. Hartung, A. M. Heidt, and H. Bartelt, "Design of all-normal dispersion microstructured optical fibers for pulse-preserving supercontinuum generation," *Opt. Exp.*, vol. 19, no. 8, pp. 7742–7749, 2011.

[13] C. C. Wang, M. H. Wang, and J. Wu, "Heavily germanium-doped silica fiber with a flat normal dispersion profile," *IEEE Photon. J.*, vol. 7, no. 2, Apr. 2015, Art. no. 7101110.

[14] M. Klimczak *et al.*, "Coherent supercontinuum generation up to 2.3 μm in all-solid soft-glass photonic crystal fibers with flat all-normal dispersion," *Opt. Exp.*, vol. 22, no. 15, pp. 18 824–18 832, 2014.

[15] T. Martynkien, D. Pysz, R. Stępień, and R. Buczyñski, "All-solid microstructured fiber with flat normal chromatic dispersion," *Opt. Lett.*, vol. 39, no. 8, pp. 2342–2345, 2014.

[16] C. L. Huang *et al.*, "Ultraflat, broadband, and highly coherent supercontinuum generation in all-solid microstructured optical fibers with all-normal dispersion," *Photon. Res.*, vol. 6, no. 6, pp. 601–608, 2018.

[17] M. Klimczak *et al.*, "Coherent supercontinuum generation in tellurite glass regular lattice photonic crystal fibers," *JOSA B*, vol. 36, no. 2, pp. A112–A124, 2019.

[18] T. S. Saini, N. P. T. Hoa, T. H. Tuan, X. Luo, T. Suzuki, and Y. Ohishi, "Tapered tellurite step-index optical fiber for co-herent near-to-mid-IR supercontinuum generation: Experiment and modeling," *Appl. Opt.*, vol. 58, no. 2, pp. 415–421, 2019.

[19] T. S. Saini, A. Kumar, and R. K. Sinha, "Broadband mid-infrared supercontinuum spectra spanning 2–15 μm using As2Se3 chalcogenide glass triangular-core graded-index photonic crystal fiber," *J. Lightw. Technol.*, vol. 33, no. 18, pp. 3914–3920, 2015.

[20] C. C. Wang and J. Li, "Saturable absorber based on the CS$_2$-filled dual-core fiber coupler," *Opt. Exp.*, vol. 26, no. 17, pp. 22144–22159, 2018.

[21] D. Churin, T.N. Nguyen, K. Kieu, R. A. Norwood, and N. Peyghambarian, "Mid-IR supercontinuum generation in an integrated liquid-core optical fiber filled with CS$_2$," *Opt. Materials Exp.*, vol. 3, no. 9, pp. 1358–1364, 2013.

[22] S. Kedenburg, T. Gissibl, T. Steinle, A. Steinmann, and H. Giessen, "Towards integration of a liquid-filled fiber capillary for supercontinuum generation in the 1.2–2.4 μm range," *Opt. Exp.*, vol. 23, no. 7, pp. 8281–8289, 2015.

[23] C. C. Wang and M. Bache, "Coherent near-Mid-IR supercontinuum generation in highly nonlinear multi-cladding liquid-core fiber designed for flat normal dispersion," in *Proc. Eur. Conf. Lasers Electro-Opt.*, Munich, Germany, Jun. 21–25, 2015.

[24] C. Wang, Y. F. Guo, L. Wei, and Z. H. Shou, "Highly coherent supercontinuum generation in CS$_2$-infiltrated single-core optical fiber," *J. Opt.*, vol. 21, no. 10, 2019, Art. no. 105501.

[25] R. Zhang, J. Teipel, and H. Giessen, "Theoretical design of a liquid-core photonic crystal fiber for supercontinuum generation," *Opt. Exp.*, vol. 14, no. 15, pp. 6800–6812, 2006.

[26] C. C. Wang, W. M. Li, N. Li, and W. Q. Wang, "Numerical simulation of coherent visible-to-near-infrared supercontinuum generation in the CHCl$_3$-filled photonic crystal fiber with 1.06 μm pump pulses," *Opt. Laser Technol.*, vol. 88, pp. 215–221, 2017.

[27] R. Song, J. Hou, S. Chen, W. Yang, and Q. Lu, "High power supercontinuum generation in a nonlinear ytterbium-doped fiber amplifier," *Opt. Lett.*, vol. 37, no. 9, pp. 1529–1531, 2012.

[28] Y. Kwon, K. Park, S. Hong, and Y. Jeong, "Numerical study on the supercontinuum generation in an active highly nonlinear photonic crystal fiber with flattened all-normal dispersion," *IEEE J. Quantum Electron.*, vol. 53, no. 5, pp. 1–8, Oct. 2017.

[29] X. Luo, T. H. Tuan, T. Suzuki, and Y. Ohishi, "Intracavity supercontinuum generation in a mode-locked erbium-doped fiber laser based on the mamyshev mechanism with highly nonlinear fiber," *Opt. Lett.*, vol. 45, no. 9, pp. 2530–2533, 2020.

[30] X. M. Liu and M. Pang, "Revealing the buildup dynamics of harmonic mode-locking states in ultrafast lasers," *Laser Photon. Rev.*, vol. 13, 2019, Art. no. 1800333.

[31] X. M. Liu, X. K. Yao, and Y. D. Cui, "Real-time observation of the buildup of soliton molecules," *Phys. Rev. Lett.*, vol. 121, no. 2, 2018, Art. no. 023905.

[32] X. M. Liu, D. Popa, and N. Akhmediev, "Revealing the transition dynamics from q switching to mode locking in a soliton laser," *Phys. Rev. Lett.*, vol. 123, no. 9, 2019, Art. no. 093901.

[33] A. Samoc, "Dispersion of refractive properties of solvents: Chloroform, toluene, benzene, and carbon disulfide in ultraviolet, visible, and near-infrared," *J. Appl. Phys.*, vol. 94, no. 9, pp. 6167–6174, 2003.

[34] J. W. Fleming, "Dispersion in GeO$_2$–SiO$_2$ glasses," *Appl. Opt.*, vol. 23, no. 24, pp. 4486–4493, 1984.

[35] G. P. Agrawal, *Nonlinear Fiber Optics*. New York, NY, USA: Academic, 2006.

[36] Y. Yuri and A. Mavritsky, "D-scan measurement of nonlinear refractive index in fibers heavily doped with GeO$_2$," *Opt. Lett.*, vol. 32, no. 22, pp. 3257–3259, 2007.

[37] M. Reichert *et al.*, "Temporal, spectral, and polarization dependence of the nonlinear optical response of carbon disulfide," *Optica*, vol. 3, no. 6, pp. 657–658, 2014.

[38] M. Chemnitz *et al.*, "Hybrid soliton dynamics in liquid-core fibres," *Nat. Commun.*, vol. 8, 2017, Art. no. 42.

[39] S. Sakaguchi and S. Todoroki, "Optical properties of GeO$_2$ glass and optical fibers," *Appl. Opt.*, vol. 36, no. 27, pp. 6809–6814, 1997.

[40] J. Lægsgaard and H. Tu, "How long wavelengths can one extract from silica-core fibers?," *Opt. Lett.*, vol. 38, no. 21, pp. 4518–4521, 2013.

[41] C. R. Giles and E. Desurvire, "Modeling erbium-doped fiber amplifiers," *J. Lightw. Technol.*, vol. 9, no. 2, pp. 271–283, 1991.

[42] Q. Kang *et al.*, "Accurate modal gain control in a multimode erbium doped fiber amplifier incorporating ring doping and a simple LP01 pump configuration," *Opt. Exp.*, vol. 20, no. 19, pp. 20835–20843, 2012.

[43] P. C. Becker, N. A. Olsson, and J. R. Simpson, *Erbium Doped Fiber Amplifiers: Fundamentals and Technology*. New York, NY, USA: Academic, 1999.

[44] A. Chong, W. H. Renninger, and F. W. Wise, "Properties of normal-dispersion femtosecond fiber lasers," *J. Opt. Soc. Am. B*, vol. 25, no. 2, pp. 140–148, 2008.

[45] K. Schaarschmidt, H.W. Xuan, J. Kobelke, M. Chemnitz, I. Hartl, and M. A. Schmidt, "Long-term stable supercontinuum generation and watt-level transmission in liquid-core optical fibers," *Opt. Lett.*, vol. 44, pp. 2236–2239, 2019.

[46] C. Finot, B. Kibler, L. Provost, and S. Wabnitz, "Beneficial impact of wave-breaking for coherent continuum formation in normally dispersive nonlinear fibers," *J. Opt. Soc. Amer. B*, vol. 25, no. 11, pp. 1938–1948, 2008.

[47] H. W. Lee *et al.*, "Pressure-assisted melt-filling and optical characterization of au nano-wires in microstructured fibers," *Opt. Exp.*, vol. 19, no. 13, pp. 12180–12189, 2011.